Online internal short circuit detection for a large format lithium ion battery

Xuning Feng [a], Caihao Weng [b], Minggao Ouyang [a,*], Jing Sun [b]

[a] State Key Laboratory of Automotive Safety and Energy, Tsinghua University, Beijing 100084, China
[b] Department of Naval Architecture and Marine Engineering, University of Michigan, Ann Arbor, MI 48109, USA

HIGHLIGHTS

- Online internal short circuit (ISC) detection scheme for Li-ion battery is proposed.
- The ISC detection algorithm is addressed from parameter estimation perspective.
- The algorithm can detect early-ISC based on the voltage and temperature responses.
- The algorithm can detect early ISC wherever the ISC location inside the battery is.

ARTICLE INFO

ABSTRACT

Early detection of an internal short circuit (ISC) in lithium ion batteries has become a crucial task for battery management, as ISC is believed to be the root cause of several large format lithium ion battery fire accidents. In this paper, a scheme of on-line detection of ISC is proposed, and the online ISC detection problem is addressed from a model parameterization and parameter estimation perspective. Using a 3D electrochemical-thermal-ISC coupled model, we explore the correlation between the measured voltage, current, and temperature data and the ISC status. It is identified that the abnormal depletion in the state-of-charge (SOC) and excessive heat generation associated with ISC affect the voltage and temperature responses, and that the correlation can be captured by a properly parameterized phenomenological model. The ISC detection is then recast as a parameter estimation problem, for which a model-based estimation algorithm is proposed and evaluated. It is shown that the estimation algorithm can track the parameter variations in real-time, thereby making it feasible to track ISC incubation status or to detect instantaneously triggered ISC. Moreover, it is observed that the recorded temperature profile is not affected by the location where the ISC occurs, due to the oval shape of the temperature distribution caused by anisotropic heat conduction of the battery core. Therefore, the proposed algorithm can detect the ISC, regardless of its physical location within the battery.

© 2015 Elsevier Ltd. All rights reserved.

1. Introduction

Given their high energy/power density and extended cycle life, lithium ion batteries have become one of the most popular choices for today's more-electrified powertrain systems [1–3]. However, several recent accidents associated with battery fire have raised great public awareness and concerns of the safety issues of lithium ion batteries [4–9].

All of the batteries that were involved in the accidents reported in [6–9] have high capacity and large formats in dimension. Large format batteries are favored by manufacturers because they reduce the cell number and pack complexity in battery pack design [10], thereby improving the reliability of a battery pack [11]. However, a large format battery is more vulnerable to safety problems because it contains more stored energy. Cooling is less effective because of the lower surface/volume ratio, which leads to higher non-uniformity in the temperature distribution within the cell [11]. A local hot spot, which may be triggered by an internal short circuit (ISC), can propagate throughout the whole cell, resulting in thermal runaway and fire [11].

An ISC is believed to be the root cause of the large format lithium ion battery fire in a series of accidents of Boeing 787 Dreamliner airplanes [8,9]. In those cases, local heat generation, induced by the ISC, developed into thermal runaway in one of the large format batteries, resulting in cell-to-cell propagation and subsequent failure of the whole battery pack [8,9]. Although

there is no clear explanation on what has led to ISC in [8,9], an abundance of evidences and field experiences indicate that it takes a long incubation time before an ISC strikes [12,13]. The ISC develops slowly during the incubation period as cycling continues [13]. The ISC-induced Joule heat will not develop into thermal runaway until the equivalent ISC resistance decreases to a substantially low level [13]. Before an ISC develops into a safety threat, it must be detected effectively to prevent the ensuing thermal runaway. The long time incubation makes it possible to perform early detection of ISC.

Early detection of ISC is a great challenge for a battery management system (BMS) and several research groups have made efforts to address this challenge. TIAX reported two technologies that can detect ISC early, according to [13]. However, no substantial details are available in the public domain due to the pending patents. With normal BMS sensors, the available signals recorded are the battery voltage, temperature, and current [14]. An ISC is usually accompanied by a voltage drop due to capacity depletion and a temperature rise due to additional heat generation [15–17]. The voltage and temperature responses may be used to detect faults such as ISC [18]. However, an ISC cannot be identified directly through the voltage and temperature responses [13] especially for large format batteries [19]. Therefore, model-based algorithms are required to interpret the ISC status from the voltage and temperature signals.

Correlating the ISC with a properly parameterized phenomenological model and then identifying the related parameters to infer the incubation status of ISC is a natural approach. With an established parametric model, the ISC detection problem can be recast as a parameter estimation problem, if the ISC incubation status can be correlated with model parameters. To this end, for ISC detection, we explore two phenomenological models: the Equivalent Circuit Model (ECM) [20,21] and the Energy Balance Equation (EBE) proposed by Bernardi, Rao and Newman in [22,23]. The former model is used to predict the voltage behavior of lithium ion batteries [20,21], whereas the simplified latter model is used to calculate the temperature response [24,25]. Both models have been validated by experiments [20,26] and have been used for different applications, such as battery SOC estimation [27–31] and SOH monitoring [32–36]. However, these models have not been used for ISC detection, to the best of the authors' knowledge.

Voltage and temperature responses of an ISC battery cell from cycling are required to develop and evaluate the ISC detection algorithms. According to the literature, ISC can be experimentally created through 4 methods: (1) nail penetration [37,38]; (2) rod crush/indentation [39,40]; (3) inserting a temperature-controlled material inside the cell [17,41]; and (4) inserting metal particles inside the cell [16]. However, it is difficult to design repeatable experiments that can emulate early stage incubation of field ISC failure. Most of the methods mentioned above will trigger a serious ISC that leads to immediate thermal runaway.

For our work on ISC detection, we use data generated by a high fidelity model instead of experimental data. Extensive research performed by several groups [19,42,43] has established an electrochemical-thermal-ISC coupled model that can capture the effects of ISC on the battery's electrochemical and thermal responses; this model will be referred as the et-ISC model in this paper. The et-ISC model has the advantage of easily simulating various levels of ISC at different locations within the battery. The electrochemical model used in the et-ISC model is based on the Dualfoil or the pseudo-two-dimensional (P2D) model developed by Doyle, Fuller and Newman [44–46], and it is regarded as a benchmark criterion to evaluate the quality of other simplified models [47–50]. This model can be expanded to include thermal effects by adding heat generation and heat transfer equations [51–57]. Moreover, an equivalent resistance is connected to the

electrochemical-thermal model to simulate ISC [19,42,43]. All of the models in [43,46,52,56,57] have been validated by experimental data. Based on these models, one can establish a validated 3D electrochemical-thermal model to simulate the localized ISC inside a large format lithium ion battery cell during the ISC incubation process.

In this paper, we use a 3D electrochemical-thermal model to simulate different cases of ISC. The voltage and temperature responses of the et-ISC model are used to correlate the ISC status with the parameters in the ECM and EBE models, thereby establishing the validity of the proposed parametric approach for online detection of ISC. The model-based parameter estimation algorithm (RLS with forgetting factor in this study) is employed to transform the voltage and temperature responses into physical parameters, whose values are used for interpreting the ISC status. Various levels of ISC, including instantaneously triggered ISC and ISC at different locations within the cell, are set in the 3D electrochemical-thermal model to evaluate the proposed ISC detection method and algorithm. The numerical results indicate that model-based parameter estimation is indeed effective in detecting ISC, regardless of the physical location within the cell.

2. An overview of the detection algorithm

Fig. 1 shows the scheme of the ISC detection algorithm. Data for current (I), voltage (V), and temperature (T) are collected and used as the input for the parameter estimation algorithm. A model-based parameter estimation algorithm is used to extract the physical parameters from the profiles of voltage, temperature, and current measurement. These physical parameters include internal resistance R_1, R_2, and battery capacitance C in the ECM model and ohmic resistance R_Ω and the temperature derivative of the equilibrium potential U_T in the EBE model. By applying the RLS algorithm with a forgetting factor to the parameterized ECM and EBE models, the estimation algorithm provides the values of the key parameters R_1, R_2, C, R_Ω, and U_T. To demonstrate the utility of the ECM and EBE model for ISC detection, we must establish a correlation between the ISC status and the estimated parameters. Towards this end, and to evaluate the validity of the proposed algorithm, the et-ISC model is used to emulate various ISC scenarios in the algorithm development. In actual implementation, real-world battery data will be used instead of model-generated data.

This paper establishes the correlation between the ISC status and estimated parameters through simulation data generated by a validated 3D et-ISC model. We show that both the ECM and EBE models can be used for ISC detection, with a properly designed estimation algorithm. These two models rely on different data to interpret different physical phenomena: one focuses on electrical signals, and the other emphasizes the thermal behavior. Although each model alone can be used to detect ISC, as we demonstrate in this paper, combining the features identified using these two models will enhance the algorithm in terms of robustness against sensor failure, battery health degradation, and environmental condition changes. It will also reduce the possibility of false alarms.

In the remainder of the paper, an ISC detection algorithm for ISC detection through parameterized ECM and EBE models is developed and verified. The et-ISC model will be introduced in Section 3, the parameter estimation algorithm will be described in Section 4, and the detection results and discussion will be presented in Section 5.

3. The internal short circuit model

3.1. Overview

Fig. 2 shows the structure of the et-ISC model [19,42,43] used for ISC simulation in this paper. The geometry of the large format
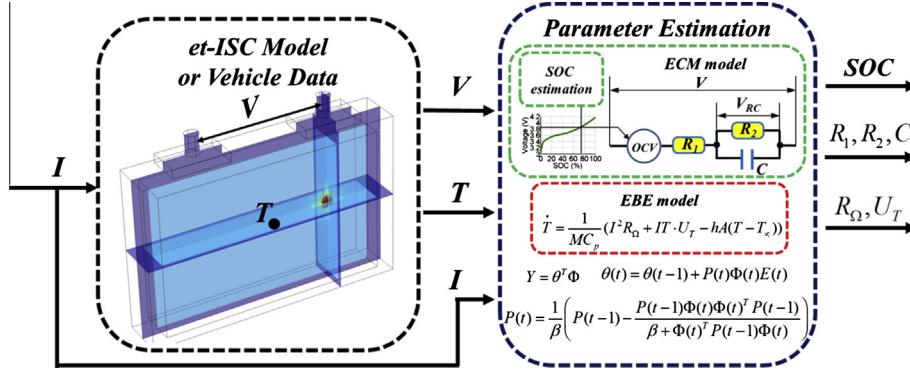
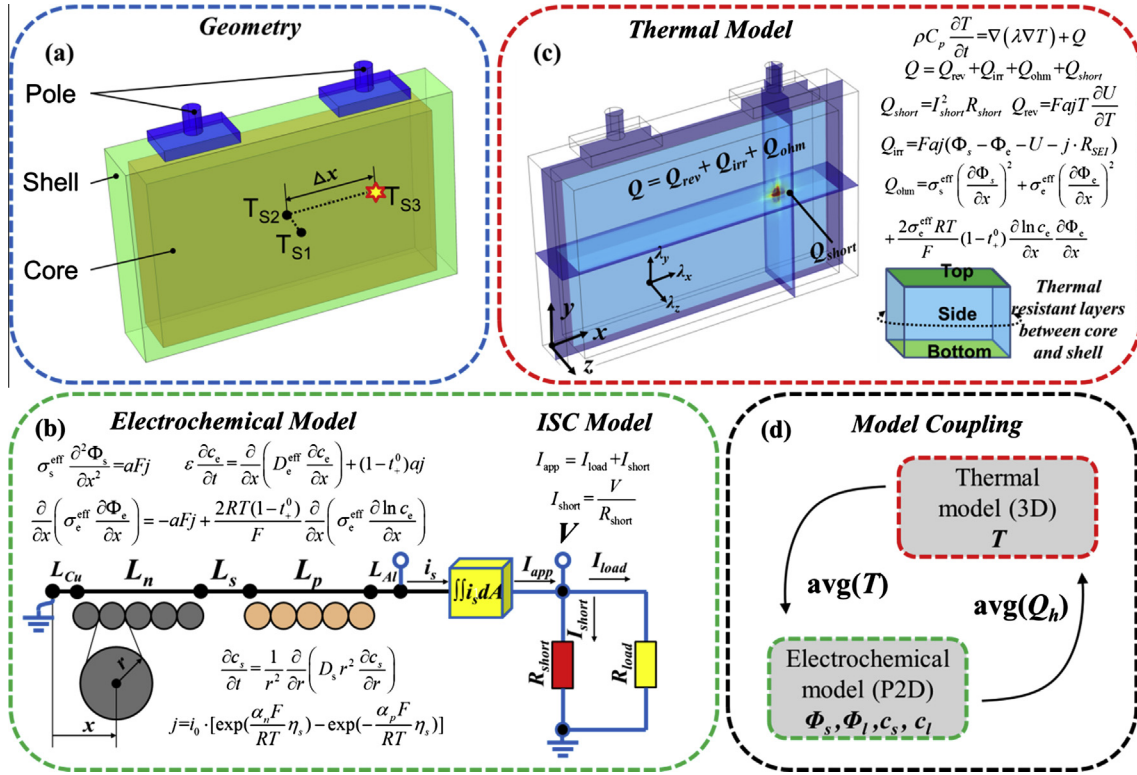**Fig. 1.** The scheme of the ISC detection algorithm.

Fig. 2. The structure of the et-ISC model in this paper.

battery to be modeled is the same as the famous PHEV-2 type standardized in DIN SPEC 91252 [58] proposed by VDA (Verband der Automobilindustrie). The physical entities include the battery core, the battery shell and the battery pole, as indicated in Fig. 2 (a). The physical dimensions of the target battery used for this study are listed in Table 1.

Table 1
The geometry of the large format battery.

Component	Symbol	Parameter name	Value (m)
Shell	L_S	Length	0.148
	B_S	Broad	0.026
	H_S	Height	0.091
Core	L_C	Length	0.130
	B_C	Broad	0.022
	H_C	Height	0.080

3.2. The pseudo-2D electrochemical model

The electrochemical model is built according to [42–57] with the governing Eqs. (1)–(10), as shown in Fig. 2(b) and listed in Table 2. The physical variables in the electrochemical model are listed in Table 3. The related physio-electrochemical parameters used in the electrochemical model are listed in Table 4. The battery is assumed to have a nominal capacity of 27 A h with a $Li_y(NiCoMn)_{1/3}O_2$ cathode and a Li_yC_6 anode, where y denotes the stoichiometry coefficients of the cathode and anode. The relationship between the open circuit potential U_{ref} and the stoichiometry coefficient y used in Eq. (10) for both the cathode and anode is shown in Fig. 3. The nominal capacity C_{norm} can be calculated by Eq. (11), where i_{1C} is the normalized current density, $A_{core} = L_C \cdot H_C$ denotes the active area of the battery core for one cell plate, $L_C(H_C)$ is the length (height) of the battery core defined in Table 1, and N is the number of stacked plates. The output voltage can be calculated by Eq. (12) as the voltage difference

Table 2
The governing equations of the electrochemical model [42–57].

Equation name	Equation expressions		Boundary conditions
Ohm's law	$-\sigma_s^{\text{eff}} \frac{\partial \Phi_s}{\partial x} = i_s$	(1)	$-\sigma_s^{\text{eff}} \frac{\partial \Phi_s}{\partial x}\big|_{x=L_{Cu}+L_n+L_s+L_p+L_{Al}} = i_{\text{app}}$
Charge, solid phase	$-\frac{\partial i_s}{\partial x} = \sigma_s^{\text{eff}} \frac{\partial^2 \Phi_s}{\partial x^2} = aFj$	(2)	$-\sigma_s^{\text{eff}} \frac{\partial \Phi_s}{\partial x}\big|_{x=L_{Cu}+L_n} = -\sigma_s^{\text{eff}} \frac{\partial \Phi_s}{\partial x}\big|_{x=L_{Cu}+L_n+L_s} = 0$
Charge, electrolyte phase	$\frac{\partial}{\partial x}\left(\sigma_e^{\text{eff}} \frac{\partial \Phi_e}{\partial x}\right) = -aFj + \frac{2RT(1-t_+^0)}{F}\frac{\partial}{\partial x}\left(\sigma_e^{\text{eff}} \frac{\partial \ln c_e}{\partial x}\right)$	(3)	$-\sigma_e^{\text{eff}} \frac{\partial \Phi_e}{\partial x}\big|_{x=L_{Cu}} = -\sigma_e^{\text{eff}} \frac{\partial \Phi_e}{\partial x}\big|_{x=L_{Cu}+L_n+L_s+L_p} = 0$
Species, solid phase	$\frac{\partial c_s}{\partial t} = \frac{1}{r^2}\frac{\partial}{\partial r}\left(D_s r^2 \frac{\partial c_s}{\partial r}\right)$	(4)	$-D_s \frac{\partial c_s}{\partial r}\big|_{r=0} = 0, \quad -D_s \frac{\partial c_s}{\partial r}\big|_{r=R_s} = j$
Species, electrolyte phase	$\varepsilon_e \frac{\partial c_e}{\partial t} = \frac{\partial}{\partial x}\left(D_e^{\text{eff}} \frac{\partial c_e}{\partial x}\right) + (1-t_+^0)aj$	(5)	$-D_e^{\text{eff}} \frac{\partial c_e}{\partial x}\big|_{x=L_{Cu}} = -D_e^{\text{eff}} \frac{\partial c_e}{\partial x}\big|_{x=L_{Cu}+L_p+L_s+L_n} = 0$
Electrical current on electrode, Butler–Volmer equation	$j = i_0 \cdot \left[\exp\left(\frac{\alpha_n F}{RT}\eta_s\right) - \exp\left(-\frac{\alpha_p F}{RT}\eta_s\right)\right]$	(6)	
Over-potential for the intercalation	$\eta_s = \Phi_s - \Phi_e - U - j \cdot R_{SEI}$	(7)	
Exchange current density	$i_0 = k \cdot (c_e)^{\alpha_n} (c_{s,\text{max}} - c_{s,e})^{\alpha_n} (c_{s,e})^{\alpha_p}$	(8)	
Local stoichiometry coefficient y for the electrode	$y = \frac{3}{R_s^3}\int_0^{R_s} r^2 \frac{c_s}{c_{s,\text{max}}} dr$	(9)	
Temperature dependent open circuit potential	$U = U_{\text{ref}}(y) - (T - T_{\text{ref}})\left[\frac{dU}{dT}\right]$	(10)	

between the positive electrode and the negative electrode in the solid phase. The voltage response of the electrochemical model can fit the experimental data of a real battery at different discharge rates, as shown in Fig. 4.

$$C_{\text{norm}} = i_{1C} \cdot A_{\text{core}} \cdot N = i_{1C} \cdot (L_C \cdot H_C) \cdot N \tag{11}$$

$$V = \Phi_s|_{x=L_{Cu}+L_n+L_s+L_p+L_{Al}} - \Phi_s|_{x=0} \tag{12}$$

3.3. The 3D thermal model

Table 5 collects all of the governing equations for the 3D thermal model according to [43,55–57]. The heat generation rate Q in Eq. (13) can be calculated by Eq. (14), where Q_{rev}, Q_{irr}, Q_{ohm}, and Q_{short} denote the reversible heat generation, irreversible heat generation, Ohmic heat generation, and the heat generation caused by ISC, respectively, and they can be calculated by Eqs. (15)–(18), according to [43,55–57]. $Q_{\text{short}} = I_{\text{short}}^2 R_{\text{short}}$ at the location where ISC occurs, whereas Q_{short} is equal to zero at other normal places without ISC. I_{short} denotes the current caused by ISC, and R_{short} denotes the equivalent resistance when ISC occurs. The detailed

Table 3
The variables in the electrochemical model.

Symbol	Description	Unit
Φ_s	Electrical potential in the solid phase	V
Φ_e	Electrical potential in the electrolyte phase	V
c_s	Insertion particle concentration in the solid phase	mol/m^3
c_e	Salt concentration in the electrolyte phase	mol/m^3
j	Molar flux	mol/m^2 s
i_s	Electrode current density	A/m^2

Table 4
The physio-electrochemical parameters used in the electrochemical model.

Symbol	Parameter	Unit	Value
C_{norm}	Nominal capacity of the large format battery	A h	27
i_{1C}	Normalized current density for 1C charge rate	A/m^2	17
N	The number of stacked plates	1	152
F	Faraday constant	A s/mol	96,485
t_+^0	Transference number	1	0.363

| Symbol	Parameter	Unit	Cu foil	Negative electrode	Separator	Positive electrode	Al foil
L	Length	M	9×10^{-6}	59×10^{-6}	25×10^{-6}	52×10^{-6}	20×10^{-6}
σ_s^{eff}	Effective electrical conductivity, solid phase	S/m	σ_s	$\varepsilon_s^{1.5}\sigma_s$		$\varepsilon_s^{1.5}\sigma_s$	σ_s
σ_s	Electrical conductivity, solid phase	S/m	5.998×10^7	100		3.8	3.774×10^7
ε_s	Volume fraction, solid phase	1		0.471		0.297	
σ_e^{eff}	Effective electrical conductivity, electrolyte phase	S/m		$\varepsilon_e^{1.5}\sigma_e$	σ_e	$\varepsilon_e^{1.5}\sigma_e$	
σ_e	Electrical conductivity, electrolyte phase	S/m		$\sigma_e = f(c_e)$ [59]	$\sigma_e = f(c_e)$	$\sigma_e = f(c_e)$	
ε_e	Volume fraction, electrolyte phase	1		0.357		0.444	
D_s	Intercalation diffusivity	m^2/s		3.9×10^{-14}		1×10^{-13}	
D_e^{eff}	Effective electrolyte diffusivity	m^2/s		$\varepsilon_e^{1.5}D_e$	D_e	$\varepsilon_e^{1.5}D_e$	
D_e	Electrolyte diffusivity	m^2/s		7.5×10^{-11}	7.5×10^{-11}	7.5×10^{-11}	
R_s	Particle radius	M		15×10^{-6}		15×10^{-6}	
A	Specific interfacial area	1/m		$3\varepsilon_s/R_s$		$3\varepsilon_s/R_s$	
α_n, α_p	Charge transfer coefficient	1		0.5		0.5	
R_{SEI}	Resistance of solid electrolyte interface	Ω m^2		0.001		0.001	
K	Reaction rate coefficient	m/s		2×10^{-11}		2×10^{-11}	
$c_{s,\text{max}}$	Maximum solid phase Li-ion concentration	mol/m^3		31,500		72,600	
Y	Stoichiometry coefficient, y at 100%/0% SOC	1		0.80/0.05		0.34/0.93	
U_{ref}	Reference open circuit potential at T_{ref} = 25 °C	V		Fig. 3		Fig. 3	
$\frac{dU}{dT}$	Temperature derivative of equilibrium potential	V/K		-0.00008		-0.0001	
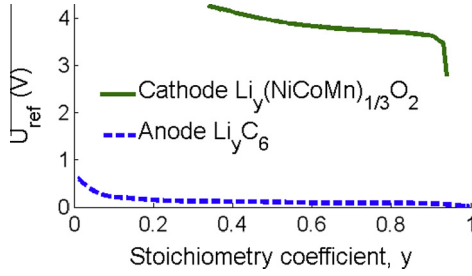
Fig. 3. The open circuit potential of the cathode and the anode for the electrochemical model.
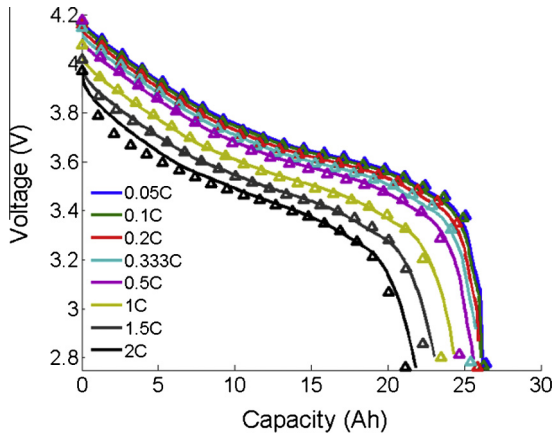

Fig. 4. A comparison of the voltage responses at different discharge rates, the electrochemical model (solid lines) and experimental data (△ markers).

treatment for ISC in both the electrochemical model and the thermal model will be discussed in Section 3.5. Thermal resistant layers, e.g., the aluminum plastic foil and the air gap, exist between the battery core and the battery shell, as shown in Fig. 2(c). The heat conductions at the thermal resistant layers are modeled by Eqs. (19) and (20).

The physical parameters used in the thermal model are listed in Table 6. The battery core is assumed to have the same anisotropic heat conductivities as in [56,60,61], the values of which are set referring to [61]. As there is always an air gap between the battery core and the battery shell in a typical battery structure, therefore a 5-mm-thick thermal resistant layer filled with air is set at the top of the battery core. The other sides and the bottom of the battery core are assumed to be wrapped by Al plastic film, referring to

the battery structure in [62]. The average heat convection coefficient is set as 5 W/m^2 K, indicating natural convection, and the ambient temperature is set as 25 °C surrounding the battery shell. The mesh grids of the 3D thermal model are shown in Fig. 5.

3.4. Coupled electrochemical-thermal model

The P2D electrochemical model and the 3D thermal model can be coupled according to Fig. 2(d), referring to [42,65]. The coupled electrochemical-thermal model is built in Comsol Multiphysics® ver 4.4. The data of temperature under different current rates are collected and are shown in Fig. 6. The model generated data can fit the experimental results with $h = 0.38$ W/m^2 K, as reported in [57], especially for the current rates less than 1C. The accuracy is deemed sufficient to simulate the temperature response in this paper because the current profiles used in subsequent sections are always less than 1C.

3.5. The ISC treatment in the model

Fig. 7 shows the ISC treatment in the electrochemical-thermal model, referring to [19,42,43]. In this study, the area of ISC is set to be 2 mm × 2 mm, located at the coordinate of $(\Delta x, \Delta y, \Delta z)$ with $(0, 0, 0)$ being the center of the battery core. The equivalent resistance of the ISC is set as R_{short}, which varies for different cases to test the detection algorithms. The ISC current, I_{short}, satisfies Ohm's law as in Eq. (21), where V is the voltage output of the model as in Eq. (12).

$$I_{\text{short}} = \frac{V}{R_{\text{short}}} \tag{21}$$

I_{short} changes the actual current profile I_{app} applied on the electrochemical model and thus influences the electrode current density i_s. I_{app} equals I_{load}, the load current, when there is no ISC, whereas I_{app} equals the sum of I_{load} and I_{short} when ISC occurs inside the battery, as in Eq. (22). I_{app} is the spatial integration of the electrode current density i_s, as in Eq. (23); therefore, I_{short} can be coupled in the electrochemical model.

$$I_{\text{app}} = \begin{cases} I_{\text{load}}, & (w/o \text{ ISC}) \\ I_{\text{load}} + I_{\text{short}}, & (w/ \text{ ISC}) \end{cases} \tag{22}$$

$$I_{\text{app}} = \iint i_s dA = N \cdot A_{\text{core}} \cdot i_s \tag{23}$$

The local heat generation caused by ISC can be calculated by Eq. (18) in Table 5. Local heat accumulation raises the temperature near the ISC point, as shown in Fig. 7. Three probes, T_{S1}, T_{S2}, and
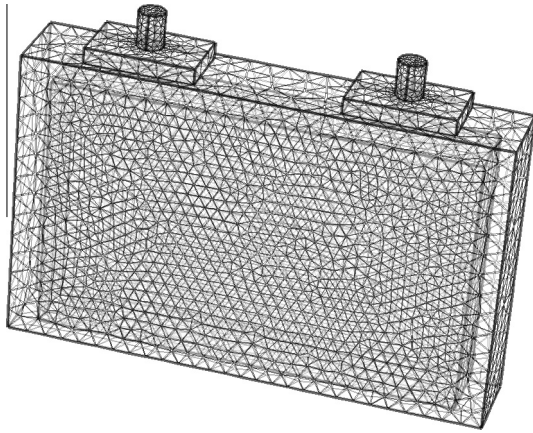
Table 5
The governing equations of the thermal model [43,55–57].

Equation name	Equation expressions		Boundary conditions
Energy balance	$\rho C_p \frac{\partial T}{\partial t} = \frac{\partial}{\partial x}\left(\lambda_x \frac{\partial T}{\partial x}\right) + \frac{\partial}{\partial y}\left(\lambda_y \frac{\partial T}{\partial y}\right) + \frac{\partial}{\partial z}\left(\lambda_z \frac{\partial T}{\partial z}\right) + Q$	(13)	$-\lambda_{\text{shell}} \frac{\partial T}{\partial n}\big|_{\text{surface}} = h(T - T_\infty)$
Heat generation	$Q = Q_{\text{rev}} + Q_{\text{irr}} + Q_{\text{ohm}} + Q_{\text{short}}$	(14)	
Reversible heat generation	$Q_{\text{rev}} = Fajt \frac{\partial U}{\partial T}$	(15)	
Irreversible heat generation	$Q_{\text{irr}} = Faj(\Phi_s - \Phi_e - U - j \cdot R_{SEI})$	(16)	
Ohmic heat generation	$Q_{\text{ohm}} = \sigma_s^{\text{eff}}\left(\frac{\partial \Phi_s}{\partial x}\right)^2 + \sigma_e^{\text{eff}}\left(\frac{\partial \Phi_e}{\partial x}\right)^2 + \frac{2\sigma_e^{\text{eff}} RT}{F}(1 - t_+^0)\frac{\partial \ln c_e}{\partial x}\frac{\partial \Phi_e}{\partial x}$	(17)	
Joule heat generation, short circuit	$Q_{\text{short}} = \begin{cases} I_{\text{short}}^2 R_{\text{short}}, & \text{short position} \\ 0, & \text{other position} \end{cases}$	(18)	
Thermal resistant layer between the core and the shell	$-\lambda_{\text{core}} \frac{\partial T}{\partial n}\big|_{\text{surface}}^{\text{core}} = \frac{\lambda_{\text{layer}}}{\delta_{\text{layer}}}(T_{\text{core}} - T_{\text{shell}})$	(19)	
	$-\lambda_{\text{shell}} \frac{\partial T}{\partial n}\big|_{\text{surface}}^{\text{core}} = \frac{\lambda_{\text{layer}}}{\delta_{\text{layer}}}(T_{\text{shell}} - T_{\text{core}})$	(20)	

Table 6
The physical parameters used in the thermal model.

Symbol	Parameter	Unit	Core	Shell	Core top	Core side & bottom	Ambience
λ_i	Thermal conductivity. The subscript $i = \{$core, shell$\}$ denotes the component in the model; $i = \{x, y, z\}$ denotes the direction of heat conduction	W/m K	$\lambda_x = \lambda_y = 21$, $\lambda_z = 0.5$ [61]	$\lambda_x = \lambda_y = \lambda_z = 160$ (Aluminum [63])			
ρ	The density	kg/m^3	2100	2700			
C_p	The specific thermal capacity	J/kg K	1100	900			
λ_{layer}	Thermal conductivity of the thin thermal resistant layer	W/m K			0.026 (air 25 °C) [64]	0.28 (Al-plastic film) [61]	
δ_{layer}	Thickness of the thin thermal resistant layer	m			0.005	0.001	
h	Convection coefficient	W/m^2 K					5
T_∞	Ambient temperature	°C					25

Fig. 5. The mesh grids of the 3D thermal model.

T_{S3}, are applied in the 3D-thermal model to monitor the temperature at the center of the battery surface, the core center, and the ISC point, respectively, as shown in Fig. 7.

The voltage and temperature measured at T_{S1} are monitored by the battery management system, as in the case of real operation. The voltage output of the model is calculated by Eq. (12), whereas the temperature output of the model is $T = T_{S1}$, which represents the temperature recorded by thermocouple placed at the surface center as in practical application.

3.6. Model responses

Fig. 8 shows the outputs of the model during 1C charge/discharge cycle with and without ISC. The equivalent resistance for ISC is $R_{short} = 20\ \Omega$. Note that the voltage response in the case of ISC is very similar to the case without ISC. Meanwhile the temperature variations are shown in both cases due to the charge/discharge activities. Therefore, direct detection of ISC through signal processing of voltage and temperature is very difficult. As a result, we pursue a model-based online parameter estimation approach to enable ISC detection.

4. The parameter estimation algorithm

4.1. Parametric model

Online parameter estimation requires a parametric model in the form of Eq. (24), where Y is the observation, θ is the parameter to be estimated, Φ is the regressor [66]. k is the time index and the sampling time is t_s from the Comsol® simulation output.

$$Y(k) = \theta(k)^T \Phi(k) \tag{24}$$

The ECM model, as shown in Fig. 1, involves the discretized Eqs. (25) and (26), where R_1, R_2 and C are the physical parameters that have correlations with the ISC status. To use the ECM model for ISC
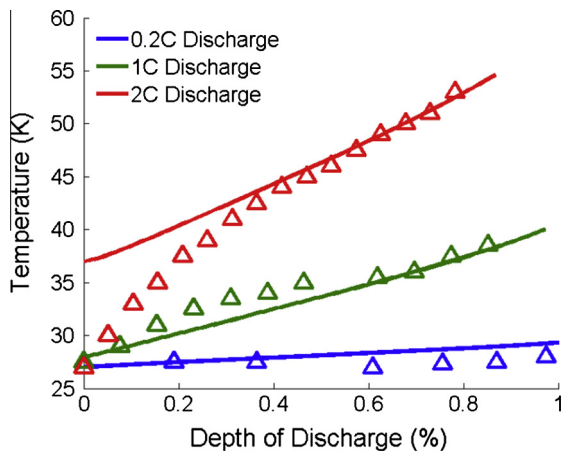
Fig. 6. A comparison of the temperature responses at different discharge rates, the thermal model (solid lines) and experimental data in [57] (Δ markers).
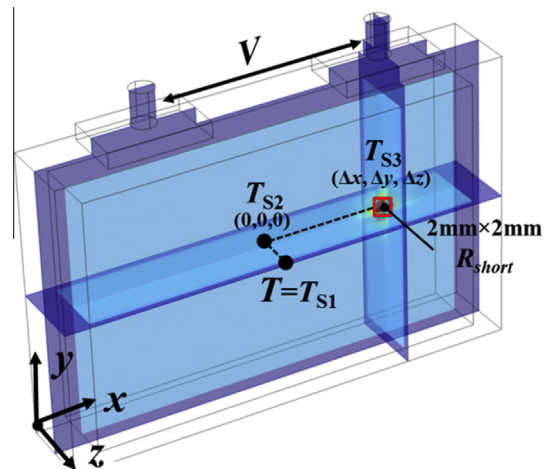
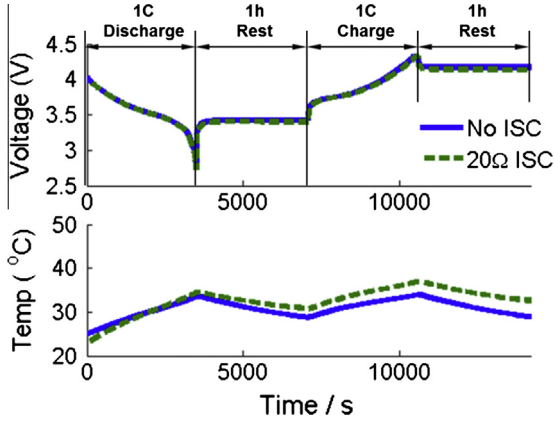**Fig. 7.** ISC settings in the electrochemical model.

Fig. 8. The output of the electrochemical-thermal model with and without ISC under 1C charge/discharge.

Table 7
The parameters used in the parameter estimation algorithm.

Symbol	Parameter	Unit	Value
t_s	The sampling time or the output time interval in Comsol simulation	s	1
M	The lumped mass of the battery	kg	0.72
C_p	The lumped specific heat capacity of the battery	J/kg K	1100
h	The lumped convective coefficient	W/m^2 K	5
A	The total surface area of the battery	m^2	0.04
T_∞	The ambient temperature	°C	25
X	The constant factor for estimating internal temperature	1	0.06
n	The points used to get the temperature derivative $\dot{T}_{S1}(k)$ by least squares	1	30
β	The forgetting factor for the RLS algorithm	1	0.999
I_{Pstop}	The current limit for covariance updating stop	A	20
Σ_V	The standard deviation of the Gaussian noise applied on the voltage signal	mV	2
Σ_T	The standard deviation of the Gaussian noise applied on the temperature signal	°C	0.1

detection, Eq. (27), representing the standard parametric model (24), is obtained by substituting Eq. (25) into (26). Next, we apply online parameter estimation of θ in the ECM model; subsequently, the estimated θ is used to determine R_1, R_2 and C.

$$V_{RC}(k) = \alpha \cdot V_{RC}(k-1) + R_2(1-\alpha) \cdot I(k-1), \ \alpha = \exp(-1/R_2C) \quad (25)$$

$$V(k) = OCV(k) - R_1 \cdot I(k) - V_{RC}(k) \quad (26)$$

$$\begin{cases} Y(k) = V(k) - OCV(k) \\ \theta(k) = (\alpha, R_1, [\alpha R_1 - R_2(1-\alpha)]) \\ \Phi(k) = ([V(k-1) - OCV(k-1)], -I(k), I(k-1)) \end{cases} \quad (27)$$

The open circuit voltage (OCV) varies with the state of charge (SOC), as shown in Fig. 9. The SOC is assumed to be calculated by Eq. (28), where SOC(k) is the estimated SOC at time $k \cdot t_s$, SOC(0) is the initial SOC, t_s is the sampling time, and $I_{SOC} = I_{load}$ when calculating the SOC. Given the relationship between the SOC and OCV, OCV is treated as known in the algorithm.

$$SOC(k) = SOC(0) + \sum_{l=1}^{k} \left(\frac{I_{SOC}(k) \cdot t_s}{C_{norm}} \right) \quad (28)$$

Similarly, given the continuous form of the EBE, as in Eq. (29), where the parameters are defined in Table 7, a parametric model for estimating R_Ω (the Ohmic resistance) and U_T (the temperature sensitivity of equilibrium potential) can be derived. The discretized form of the EBE is given by Eq. (30), where T_{S1} and T_{S2} represent the temperature at the center of the battery surface and the center of the battery core, respectively, as shown in Fig. 7. However, the internal temperature is inaccessible and only $T = T_{S1}$ can be measured in practical use. Therefore, Eq. (31) is used to calculate
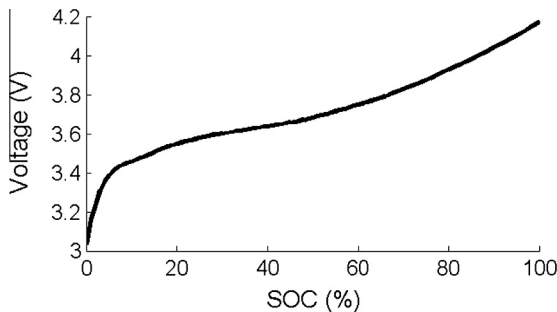

Fig. 9. OCV vs. SOC as an output of the electrochemical-thermal model.

the internal temperature of the core (T_{S2}) using T_{S1}, where the definitions and values of parameters used in Eqs. (30) and (31) are given in Table 7. Substituting Eq. (31) in (30), we obtained the standardized Y, θ, and Φ for parameter estimation in Eq. (32).

$$\dot{T} = \frac{1}{MC_p} \left(I^2 R_\Omega + IT \cdot U_T - hA(T - T_\infty) \right) \quad (29)$$

$$\dot{T}_{S2}(k) = \frac{1}{MC_p} \left(I(k)^2 \cdot R_\Omega + I(k)T_{S2}(k) \cdot U_T - hA(T_{S1}(k) - T_\infty) \right) \quad (30)$$

$$T_{S2} = T_{S1} + X(T_{S1} - T_\infty) \quad (31)$$

$$\begin{cases} Y(k) = MC_p(1+X)\dot{T}_{S1}(k) + hA(T_{S1}(k) - T_\infty) \\ \theta(k) = (R_\Omega, U_T) \\ \Phi(k) = (I^2(k), I(k) \cdot [T_{S1}(k) + X(T_{S1}(k) - T_\infty)]) \end{cases} \quad (32)$$

The temperature derivative $\dot{T}_{S1}(k)$ is not directly measured, but numerically calculated by (1) fitting 2n points nearest to time k using simple linear regression, as in Eq. (33), where a and b are derived through least squares; and (2) setting the temperature derivative $\dot{T}_{S1}(k)$ equal to the derivative a of the fitting function.

$$T_{S1}(k) = ak + b \quad (33)$$

4.2. Parameter estimation algorithm

We can employ the recursive least squares (RLS) algorithm with a forgetting factor β to estimate the parameter θ to detect the occurrence of ISC. Eqs. (24) and (34)–(37) are the standard equations for the RLS algorithm referring to [66–68].

$$Y(k) = \theta(k)^T \Phi(k)$$

$$E(k) = Y(k) - \theta(k-1)^T \Phi(k) \quad (34)$$

$$\theta(k) = \theta(k-1) + K(k)E(k) \quad (35)$$

$$K(k) = \frac{P(k-1)\Phi(k)}{\beta + \Phi(k)^T P(k-1)\Phi(k)} \quad (36)$$

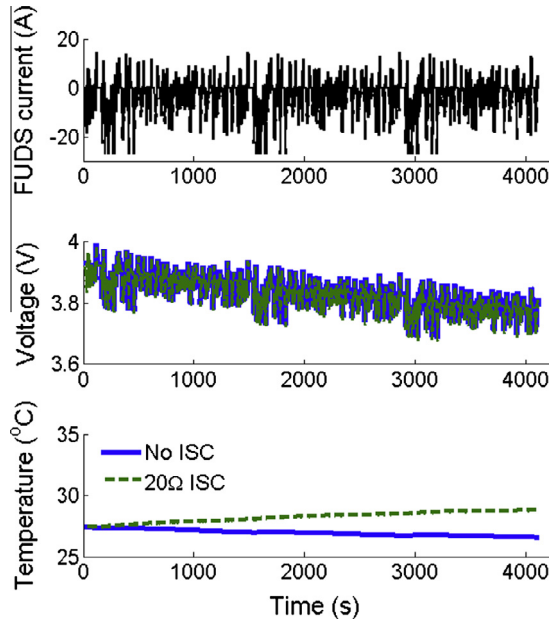$$P(k) = \frac{P(k-1) - K(k)\Phi(k)^T P(k-1)}{\beta} \quad (37)$$

Fig. 10. Model output applying FUDS current profile.

The updates of the parameter θ and the covariance P are stopped when the current $I(k) > I_{\text{Pstop}}$ for some threshold I_{Pstop}, because the model is only validated for low charging current.

$$\begin{cases} \theta(k) = \theta(k-1) \\ P(k) = P(k-1) \end{cases}, \text{ no updating when } I(k) > I_{\text{Pstop}} \text{ in the thermal}$$

$$\text{model Eqs. (29)−(32)}$$

$$(38)$$

4.3. Data for algorithm evaluation

Federal Urban Drive Cycle (FUDS) [69] is used as the current input of the ISC model to guarantee persistent excitation, a condition that will help parameter estimation. FUDS can also simulate practical working conditions of the battery. The model outputs of V and T under 3 repeated FUDS cycles is shown in Fig. 10. V and T have sampling accuracies of 1 mV and 0.01 °C, respectively. White noise with Gaussian distribution $N(0, \Sigma_V)$ and $N(0, \Sigma_T)$ have

Table 8
ISC cases for testing the detection algorithm.

Case	FUDS cycle no.	Total time [s]	R_{short} [Ω]	ISC position $(\Delta x, \Delta y, \Delta z)$ [mm]	Max$\{T = T_{S3}\}$ at ISC point [°C]
1	3	4116	∞	No ISC	27.59
2	3	4116	100	(0,0,0)	29.39
3	3	4116	50	(0,0,0)	31.21
4	3	4116	20	(0,0,0)	36.96
5	3	4116	10	(0,0,0)	48.00
6	5	6860	0 ($k \leqslant 3430$ s) 10 ($k > 3430$ s)	(0,0,0)	46.38
7	5	6860	0 ($k \leqslant 3430$ s) 20 ($k > 3430$ s)	(0,0,0)	36.44
8	3	4116	10	(0,0,−5)	49.93
9	3	4116	10	(0,0,5)	50.92
10	3	4116	10	(60,0,0)	51.47
11	3	4116	10	(60,0,−5)	51.98
12	3	4116	10	(60,0,5)	52.17
13	3	4116	10	(60,30,−5)	53.18

Table 9
Initial conditions for the ISC simulations.

	SOC(0)	x in Li$_x$C$_6$	y in Li$_y$(NiCoMn)$_{1/3}$O$_2$	Initial temperature $T(0)$ [°C]
Value	80%	0.649	0.458	27.5

been added into the sampled signal V and T to emulate practical conditions. Finally, the parameters of interest and their values used in simulation are summarized in Table 7.

5. Detection results and discussion

5.1. Overview

To evaluate the effectiveness of the model-based parameter estimation algorithm for ISC detection, data were generated by the et-ISC model for different scenarios (as in Table 8) with the following specifics: (1) Case 1–Case 5 are established with various degrees of ISC to test the capability of the algorithm in detecting different levels of ISC; (2) Case 6 and Case 7 are established to test the capability of the algorithm to detect the instantaneously-triggered ISC during cycling; and (3) Case 8–Case 13 are established to evaluate the algorithm when the ISC occurs at different locations within the battery. In addition, the initial conditions for all of the simulations are listed in Table 9.

The maximum temperature at the ISC point (T_{S3} in Fig. 7) during cycling is given in the last column of Table 8 to confirm that the cases are indeed reflecting the ISC at different incubation stages. The maximum temperature for ISC with an equivalent resistance of $R_{\text{short}} = 10\,\Omega$ is 53 °C. A higher temperature (>55 °C) may lead to severe battery capacity fading, and the self-heating could be triggered at $T > 85$ °C, as reported in [70]. Therefore, it would be helpful if early ISC can be detected when the equivalent ISC resistance is larger than 10 Ω.

5.2. Detection of ISC at various incubation stages

Cases 1–5 are established to test the capability of the algorithm in detecting different levels of ISC. Fig. 11 shows the detection results based on the ECM model using voltage measurements. The voltage curve for more severe ISC (with lower R_{short}) will be slightly lower than those with less severe ISC, as shown in Fig. 11(a), due to the extra SOC depletion associated with ISC. Fig. 11(b) shows the estimation results for the parameters in the ECM model using Eqs. (24), (27), and (34)–(37). The values for the estimated R_1, R_2, and C are listed in Table 10. As shown in Fig. 11(b) and Table 10, as R_{short} decreases, R_1 changes slightly, indicating minor changes in the DC resistance during ISC. The values of R_2 and C increase 355% and 78% (173% and 35%), respectively, for the ISC resistance $R_{\text{short}} = 10\,\Omega$ (20 Ω). The excessive increments of R_2 and C are caused by the accumulating voltage depletion due to ISC. The results indicate that the algorithm may detect ISC based on the ECM when R_{short} is as high as 20 Ω.

Fig. 12(a) shows the 3-D temperature distributions for Case 1 (no ISC) and Case 4 ($R_{\text{short}} = 20\,\Omega$) before and after 3 FUDS cycles. A hot spot caused by local ISC heating can be seen at the center of the battery core for Case 4. Fig. 12(b) compares the temperature responses for Cases 1–5. The center temperature (T_{S2} in Fig. 7) shows different levels of temperature rise with different R_{short}, whereas the surface temperature curves show some drifts with different temperature rise/drop rates. Fig. 12(c) is the detection results based on the EBE model, Eqs. (24), (32), and (34)–(38).
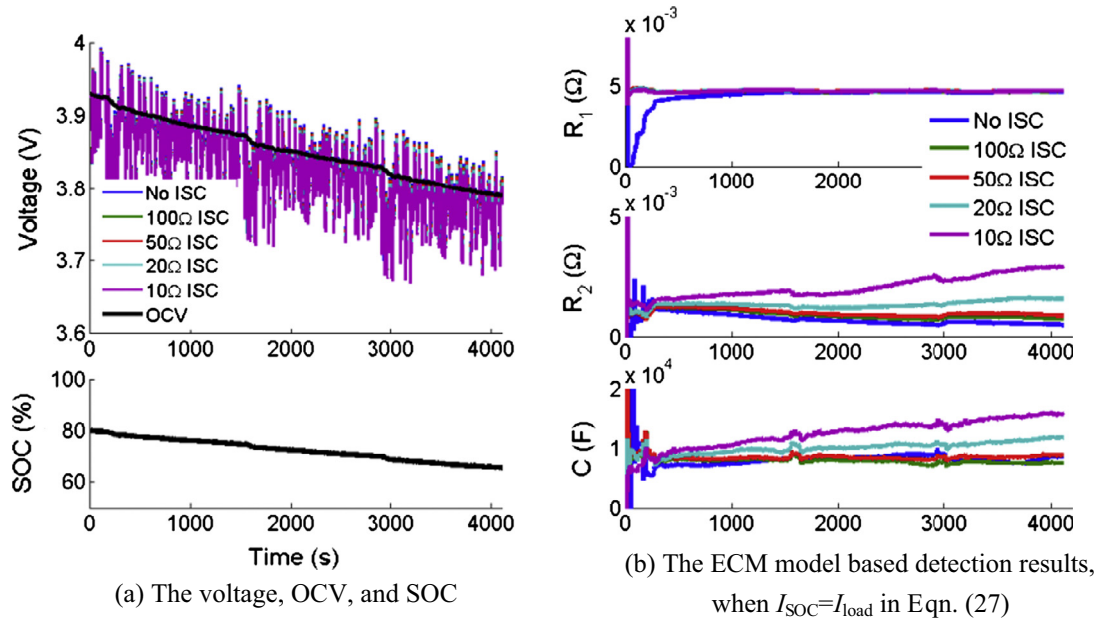
(a) The voltage, OCV, and SOC

(b) The ECM model based detection results, when $I_{SOC}=I_{load}$ in Eqn. (27)

Fig. 11. Voltage-related detection results for various degree of ISC.

Table 10
Detection results for various degrees of ISC.

Case	R_{short} [Ω]	Average value in the last FUDS cycle, $k \in [2745, 4116]$ s				
		R_1 [mΩ]	R_2 [mΩ]	C [F]	R_Ω [mΩ]	U_T [mV/K]
1	∞	4.6	0.55	8158	1.4	−0.0153
2	100	4.7	0.78	7528	2.2	−0.0230
3	50	4.7	0.91	8522	2.9	−0.0255
4	20	4.7	1.50	11,003	4.8	−0.0660
5	10	4.7	2.50	14,544	8.3	−0.1128

As shown in Fig. 12(c) and Table 10, as R_{short} decreases, the absolute values of R_Ω and U_T, which represent the average heat generation during operation, show obvious increases due to the excessive heat generation caused by the ISC. The absolute values of R_Ω and U_T increase 493% and 637% (243% and 331%), respectively, for the ISC resistance $R_{short} = 10\,\Omega(20\,\Omega)$. In addition, observable increases (67% and 107%) in the absolute values of R_Ω

and U_T, respectively, for $R_{short} = 50\,\Omega$ indicates that the algorithm may detect ISC based on the EBE, even when R_{short} is as high as $50\,\Omega$.

The results establish that both models can be used for ISC detection, with EBE having higher sensitivity for mild ISC cases.

5.3. Detection of instantaneously triggered ISC

For Case 6 and Case 7, the et-ISC model is established to test the capability of the algorithm to detect an instantaneously triggered ISC during cycling. The ISC is presumed to be triggered at time $t = 3431$ s. Fig. 13(a) illustrates that no local hot spot occurs inside the battery between 0 and 3430 s in the simulation of Case 6, whereas a continuous temperature rise is observed once the ISC is triggered. Fig. 13(b) shows the voltage and temperature responses for Case 6 and Case 7. The temperature at the battery center (T_{S2} in Fig. 7) rises sharply, whereas the surface
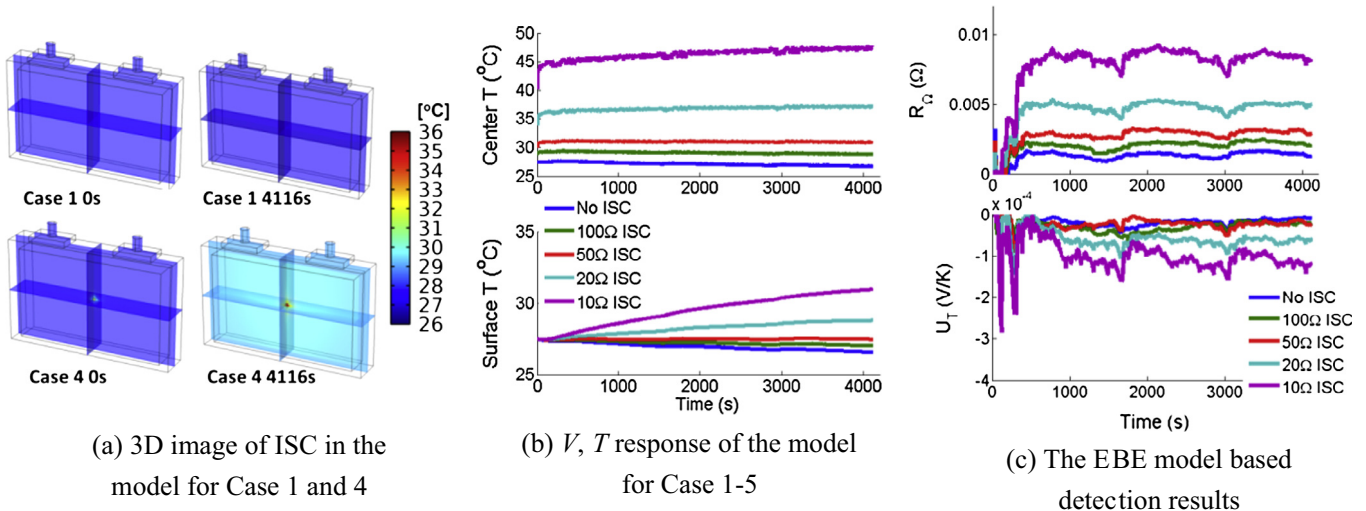

(a) 3D image of ISC in the model for Case 1 and 4

(b) V, T response of the model for Case 1-5

(c) The EBE model based detection results

Fig. 12. Temperature-related detection results for various degree of ISC.

(a) 3D image of ISC in the model for Case 6

(b) V, T response of the model for Case 6 and 7

(c) Detection results based on the ECM model

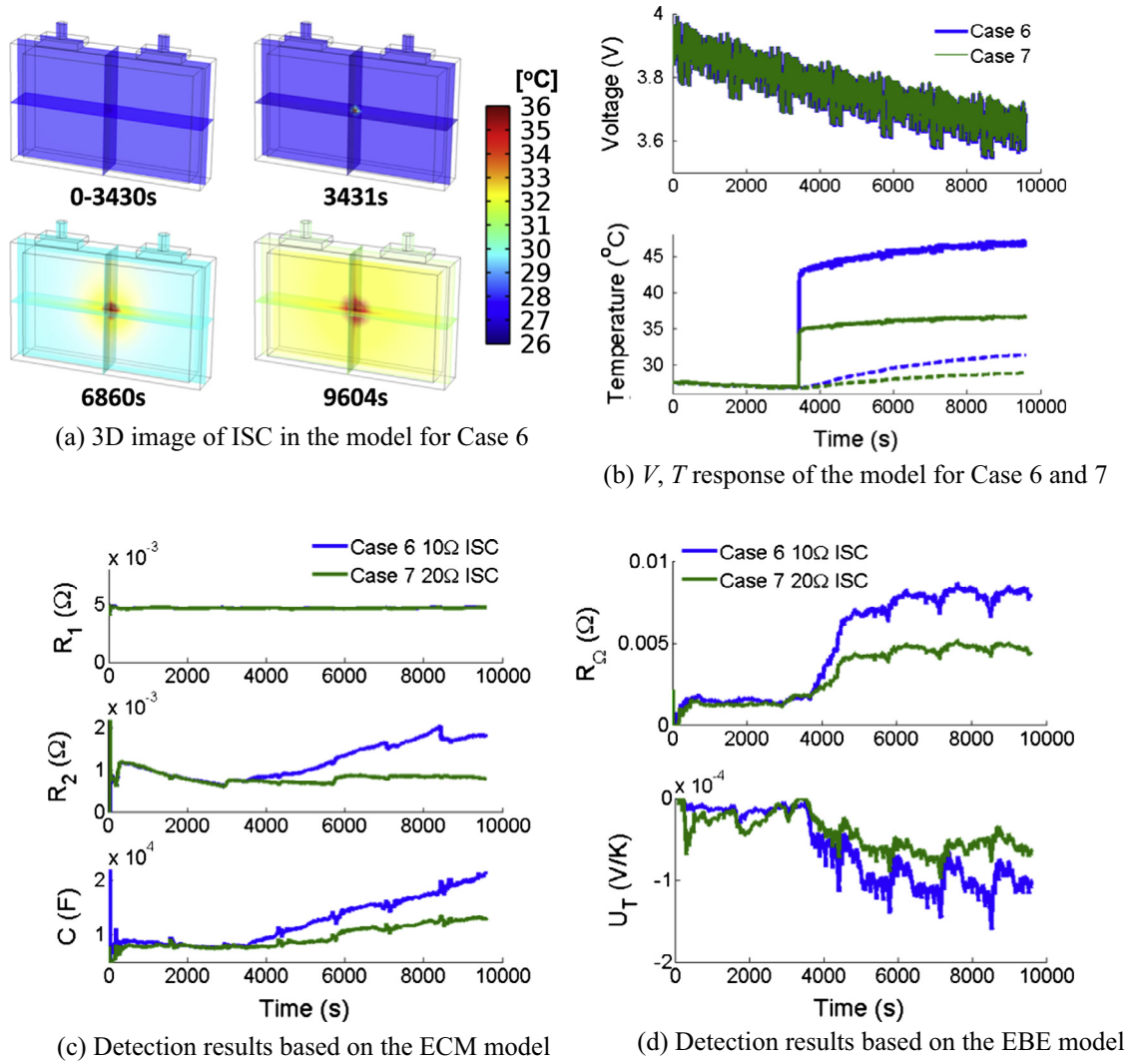(d) Detection results based on the EBE model

Fig. 13. Detection results instantaneously triggered ISC.

Table 11
Detection results for instantaneously triggered ISC.

Case	FUDS cycle no.	Average value in one FUDS cycle				
		R_1 [mΩ]	R_2 [mΩ]	C [F]	R_Ω [mΩ]	U_T [mV/K]
6	1	/	/	/	/	/
	2	4.7	0.78	7939	1.5	−0.017
	3	4.7	0.75	8313	1.9	−0.027
	4	4.6	0.95	11,266	6.1	−0.081
	5	4.6	1.40	14,372	7.6	−0.101
	6	4.7	1.70	16,268	8.0	−0.101
	7	4.7	1.80	19,442	7.9	−0.104
7	1	/	/	/	/	/
	2	4.7	0.76	7827	1.2	−0.028
	3	4.7	0.71	7731	1.7	−0.018
	4	4.6	0.69	8508	3.8	−0.050
	5	4.6	0.81	10,478	4.6	−0.064
	6	4.6	0.84	11,571	4.7	−0.064
	7	4.7	0.83	12,656	4.7	−0.055

temperature ($T = T_{S1}$ in Fig. 7) starts to rise slowly when ISC is triggered. The estimation results of the algorithm can adapt to the instantaneously triggered ISC, as shown in Fig. 13(c), (d) and Table 11. The values of R_2 and C increase by 131% and

145% (9% and 62%), respectively, and the average absolute values of R_Ω and U_T in one FUDS cycle increase 433% and 494% (96% and 292%), respectively, after ISC is triggered for $R_{short} = 10\,\Omega$ (20 Ω). The EBE model-based algorithm detects the instantaneously
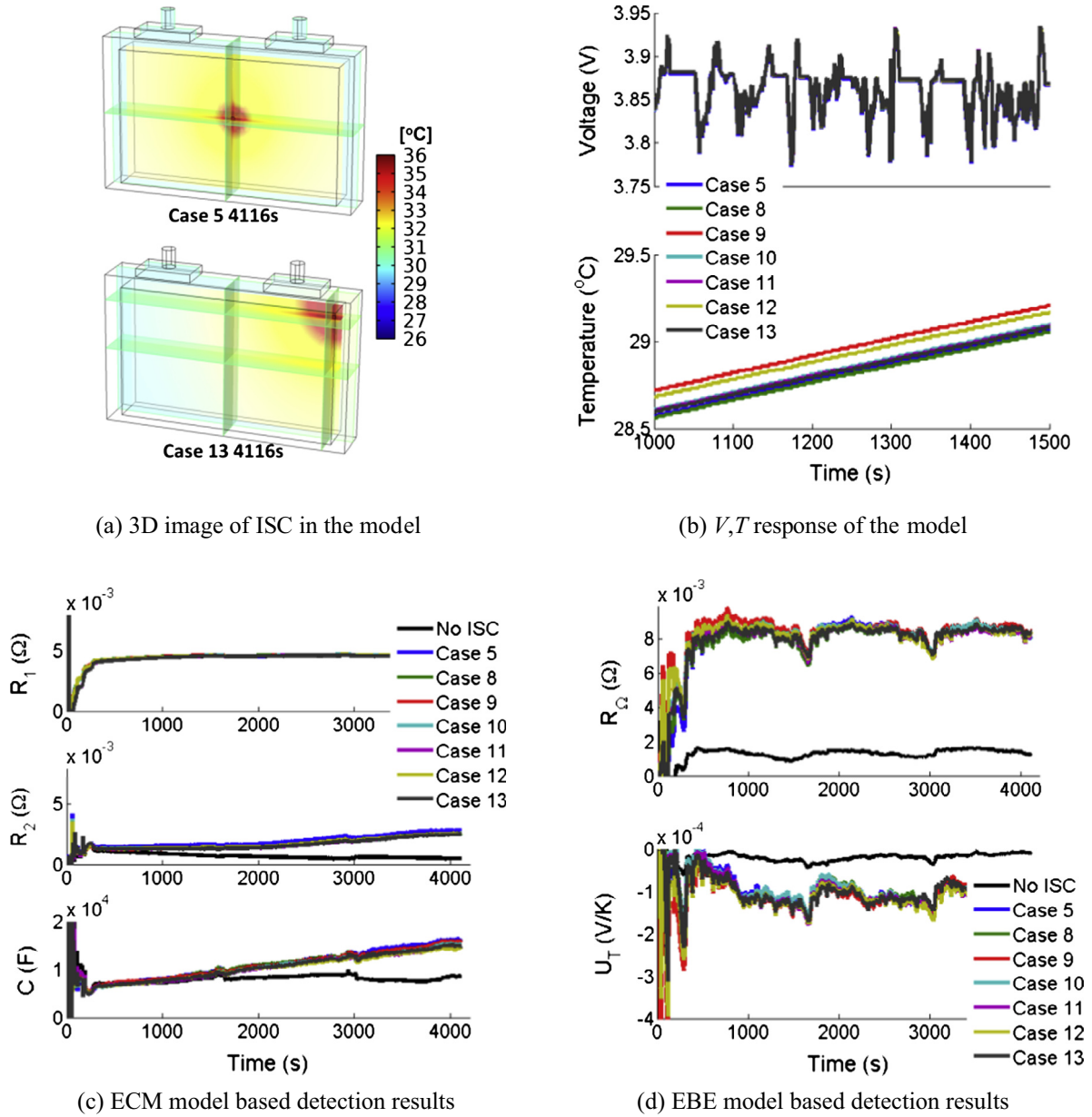
(a) 3D image of ISC in the model

(b) V,T response of the model

(c) ECM model based detection results

(d) EBE model based detection results

Fig. 14. Detection results for ISC at different locations.

Table 12
Detection results for ISC at different locations.

Case	Average value in the last FUDS cycle, $k \in [2745, 4116]$ s				
	R_1 [mΩ]	R_2 [mΩ]	C [F]	R_Ω [mΩ]	U_T [mV/K]
1	4.6	0.55	8158	1.4	−0.0153
5	4.7	2.50	14,544	8.3	−0.1128
8	4.7	2.30	13,784	8.3	−0.1050
9	4.7	2.20	14,135	8.5	−0.1048
10	4.7	2.20	13,620	8.4	−0.1103
11	4.7	2.20	13,272	8.2	−0.1143
12	4.7	2.30	13,167	8.2	−0.1185
13	4.6	2.20	13,583	8.4	−0.1035

triggered ISC more quickly than the ECM-based algorithm when ISC is instantaneously triggered.

5.4. Detection of ISC at different locations

The 3D et-ISC model provides a convenient means for us to investigate the effects of ISC when it occurs at different locations within a cell. Case 5 and Cases 8–13 provide simulation results corresponding to ISC at different locations. We choose $R_{short} = 10\,\Omega$ because in this case, the ISC can cause the most severe non-uniformity of temperature distribution. Fig. 14(a) illustrates the temperature distribution at the end of 3 FUDS cycles for Case 5 and Case 13. The maximum temperature of Case 13 (53.18 °C) is slightly higher than that of Case 5 (48.00 °C), because the heat dissipation at the corner is poorer than at the center, as reported in [37]. Fig. 14(b) shows the voltage and temperature responses for Case 5 and Cases 8–13. The voltage responses are quite similar, which leads to similar estimation results based on the ECM model, as shown in Fig. 14(c) and Table 12. There is at most a 0.2 °C difference in temperature responses at the battery surface. Moreover,
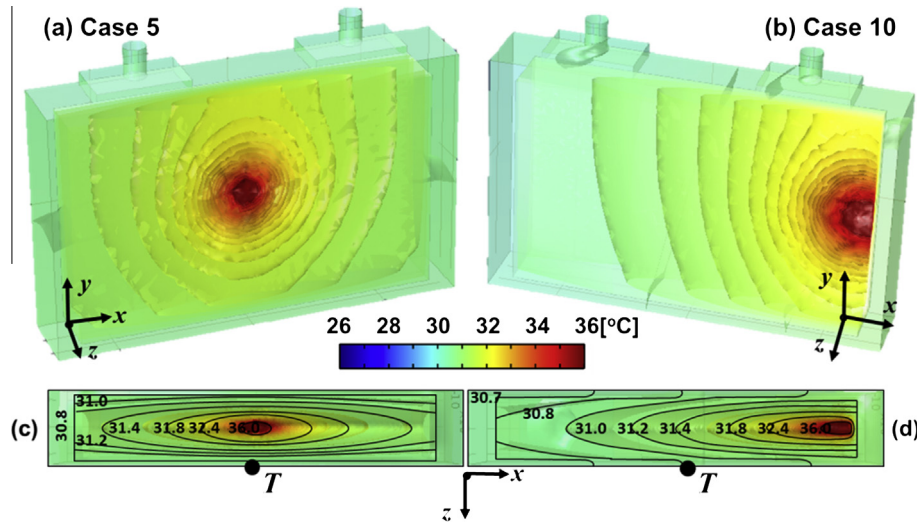
Fig. 15. Oval temperature distribution in the battery core.

the temperature rise rates are similar, indicating similar inputs of $\dot{T}_{S1}(k)$ and $Y(k)$ as those in (32); therefore, the estimation results based on the EBE model are quite close, as presented in Fig. 14 (d) and Table 12.

Fig. 15 helps explain the reason for the similar temperature responses for cases with ISC at different locations. Fig. 15(a) and (b) shows the temperature distributions for Case 5 and Case 10, respectively, at the end of 3 FUDS cycles (t = 4116 s). The anisotropic thermal conductivity of the battery core ($\lambda_x = \lambda_y$ = 21 W/m K and λ_z = 0.5 W/m K in Table 6) leads to an ellipsoid temperature distribution surrounding the ISC point, as shown in Fig. 15(a) and (b). Therefore, the oval isothermal line in the intersection $x - z$ plane at $y = 0$ leads to similar responses of the surface temperature $T = T_{S1}$, as illustrated in Fig. 15(c) and (d). Here, in Fig. 15(c) and (d), for both cases, the temperature $T = T_{S1}$ recorded at the battery surface is approximately 30.8 °C according to the isothermal line.

In summary, with only one temperature sensor T_{S1} located at the center of the battery surface, the proposed detection algorithm leads to similar detection results, regardless of the ISC locations. This result is an advantage of the proposed algorithm, in the sense that we do not need to incorporate the location sensitivity in the algorithm development. If, however, one wishes to detect not only the ISC status but also its location, then more temperature sensors must be installed at different locations on the battery surface.

6. Conclusion

This paper investigated the detectability of ISC in a large format lithium ion battery for BMS using only the measurements of current, voltage, and temperature (at the center of the battery surface). We demonstrated a successful ISC detection algorithm through a model-based parameter estimation algorithm.

A 3D electrochemical-thermal model was built to simulate various ISC scenarios inside a large format lithium ion battery. The model can predict the voltage and temperature responses of the battery with or without ISC. The RLS algorithm with forgetting factor was applied to estimate the critical parameters in the parameterized ECM and the EBE models. The changes in the estimated parameters, namely the parallel-connected R_2 and C in ECM, ohmic resistance R_Ω and temperature derivative of equilibrium potential U_T in EBE, can be used as indicators of ISC. The same algorithm can detect the ISC status in the incubation process or the ISC that is triggered instantaneously. We also showed that an ISC can be detected regardless of where it occurs using the temperature measured at the surface center. To detect the ISC location within a large format lithium ion battery, additional sensors must be employed.

Our future research on ISC detection will focus on the following: (1) conducting experiments to validate the ISC detection algorithm; and (2) characterizing optimized temperature sensor placement to detect the ISC location.

References

[1] Xue N, Du W, Greszler TA, Shyy W, Martins JRRA. Design of a lithium-ion battery pack for PHEV using a hybrid optimization method. Appl Energy 2014; 115:591–602.
[2] Ping P, Wang Q, Huang P, Sun J, Chen C. Thermal behavior analysis of lithium-ion battery at elevated temperature using deconvolution method. Appl Energy 2014;129:261–73.
[3] Wang T, Tseng KJ, Zhao J, Wei Z. Thermal investigation of lithium-ion battery module with different cell arrangement structures and forced air-cooling strategies. Appl Energy 2014;134:229–38.
[4] Wang Q, Ping P, Zhao X, Chu G, Sun J, Chen C. Thermal runaway caused fire and explosion of lithium ion battery. J Power Sources 2011;196:210–24.
[5] Beauregard GP. Report of investigation: hybrids plus plug in hybrid electric vehicle. eTec, Phoenix, AZ. Tech rep; June 26, 2008.
[6] Smith B. Chevrolet volt battery incident summary report. National Highway Traffic Safety Administration, DC. Rep no. DOT-HS-811-573; January 20, 2012.
[7] Willard N, He W, Hendricks C, Pecht M. Lessons learned from the 787 Dreamliner issue on lithium-ion battery reliability. Energies 2013;6:4682–95.
[8] Aircraft incident report: auxiliary power unit battery fire. Japan airlines Boeing 787, JA 829J, Boston, Massachusetts, January 7, 2013. National Transportation Safety Board, DC. Rep no. PB2014-108867; November 21, 2014.
[9] Goto N. Aircraft serious incident investigation report: all Nippon Airways Co. Ltd. JA804A. Japan Transport Safety Board, Tokyo, Japan. Rep no. AI2014-4; September 25, 2014.
[10] Lee KJ, Smith K, Pesaran A, Kim GH. Three dimensional thermal-, electrical-, and electro chemical-coupled model for cylindrical wound large format lithium-ion batteries. J Power Sources 2013;241:20–32.
[11] Kim GH, Pesaran A, Spotnitz R. A three-dimensional thermal abuse model for lithium-ion cells. J Power Sources 2007;170:476–89.

[12] Doughty DH, Pesaran A. Vehicle battery safety roadmap guidance. National Renewable Energy Laboratory, Golden, CO, Subcontract rep no. NREL/SR-5400-54404; October 2012.

[13] Barnett B. Technologies for detection and intervention of internal short circuits in Li-ion batteries. In: Presented at the 5th annual knowledge foundation conf battery safety 2014, Washington D.C., US; November 11–14, 2014.

[14] Lu L, Han X, Li J, Hua J, Ouyang M. A review on the key issues for lithium-ion battery management in electric vehicles. J Power Sources 2013;226:272–88.

[15] Ramadass P, Fang W, Zhang Z. Study of internal short in a Li-ion cell I: test method development using infra-red imaging technique. J Power Sources 2014;248:769–76.

[16] Santhanagopalan S, Ramadass P, Zhang Z. Analysis of internal short-circuit in a lithium ion cell. J Power Sources 2009;194:550–7.

[17] Orendorff CJ, Roth EP, Nagasubramanian G. Experimental triggers for internal short circuits in lithium-ion cells. J Power Sources 2011;196:6554–8.

[18] Xia B, Chen Z, Mi C, Robert B. External short circuit fault diagnosis for lithium ion batteries. In: Presented at transportation electrification conference and expo (ITEC), Deaborn, MI, US; 2014. p. 1–7.

[19] Kim GH, Smith K, Ireland J, Pesaran A. Fail-safe design for large capacity lithium-ion battery systems. J Power Sources 2012;210:243–53.

[20] Hu X, Li S, Peng H. A comparative study of equivalent circuit models for Li-ion batteries. J Power Sources 2012;198:359–67.

[21] Liaw BY, Nagasubramanian G, Jungst RG, Doughty DH. Modeling of lithium ion cells – a simple equivalent-circuit model approach. Solid State Ionics 2004;175:835–9.

[22] Bernardi D, Pawikowski E, Newman J. A general energy balance for battery systems. J Electrochem Soc 1985;132(1):5–12.

[23] Rao L, Newman J. Heat-generation rate and general energy balance for insertion battery systems. J Electrochem Soc 1997;144(8):2697–704.

[24] Chen Y, Evans JW. Heat transfer phenomena in lithium/polymer-electrolyte batteries for electric vehicle application. J Electrochem Soc 1993;140(7):1833–8.

[25] Chen SC, Wang YY, Wan CC. Thermal analysis of spirally wound lithium batteries. J Electrochem Soc 2006;153(4):A637–48.

[26] Liu G, Ouyang M, Lu L, Li J, Han X. Analysis of the heat generation of lithium-ion battery during charging and discharging considering different influencing factors. J Therm Anal Calorim 2014;116:1001–10.

[27] Xiong R, Sun F, He H, et al. A data-driven adaptive state of charge and power capability joint estimator of lithium-ion polymer battery used in electric vehicles[J]. Energy 2013;63:295–308.

[28] Dai H, Wei X, Sun Z, Wang J, Gu W. Online cell SOC estimation of Li-ion battery packs using a dual time-scale Kalman filtering for EV applications. Appl Energy 2012;95:227–37.

[29] Weng C, Sun J, Peng H. A unified open-circuit-voltage model of lithium-ion batteries for state-of-charge estimation and state-of-health monitoring. J Power Sources 2014;258:228–37.

[30] Xing Y, He W, Pecht M, Tsui KL. State of charge estimation of lithium-ion batteries using the open-circuit voltage at various ambient temperatures. Appl Energy 2014;113:106–15.

[31] Sun F, Xiong R, He H. Estimation of state-of-charge and state-of-power capability of lithium-ion battery considering varying health conditions. J Power Sources 2014;259:166–76.

[32] Waag W, Kaebitz S, Sauer DU. Experimental investigation of the lithium ion battery impedance characteristic of various conditions and aging status and its influence on the application. Appl Energy 2013;102:885–97.

[33] Chiang YH, Sean WY, Ke JC. Online estimation of internal resistance and open-circuit voltage of lithium-ion batteries in electric vehicles. J Power Sources 2011;196:3921–32.

[34] Fleischer C, Waag W, Heyn H, Sauer DU. Online adaptive battery impedance parameter and state estimation considering physical principles in reduced order equivalent circuit battery models: Part 2. Parameter and state estimation. J Power Sources 2014;262:457–82.

[35] Plett GL. Extended Kalman filtering for battery management systems of LiPB-based HEV battery packs, Part 3. State and parameter estimation. J Power Sources 2004;134:277–92.

[36] Lin X, Perez HE, Siegel JB, Stefanopoulou AG. Online parameterization of lumped thermal dynamics in cylindrical lithium ion batteries for core temperature estimation and health monitoring. IEEE Trans Control Syst Technol 2013;21(5):1745–55.

[37] Maleki H, Howard JN. Internal short circuit in Li-ion cells. J Power Sources 2009;191:568–74.

[38] Feng X, Sun J, Ouyang M, Wang F, He X, Lu L, et al. Characterization of penetration induced thermal runaway propagation process within a large format lithium ion battery module. J Power Sources 2015;275:261–73.

[39] Lamb J, Orendorff CJ. Evaluation of mechanical abuse techniques in lithium ion batteries. J Power Sources 2014;247:189–96.

[40] Sahraei E, Campbell J, Wierzbicki T. Modeling and short circuit detection of 18650 Li-io cells under mechanical abuse conditions. J Power Sources 2012;220:360–72.

[41] Keyser M, Long D, Ireland J, Pesaran A, Darcy E, Shoesmith M, et al. Internal short circuit instigator in lithium ion cells. In: Presented at the 4th annual knowledge foundation conf battery safety 2013, San Diego, CA; November 14, 2013.

[42] Zhao W, Luo G, Wang CY. Modeling nail penetration process in large-format Li-ion cells. J Electrochem Soc 2014;162(1):A207–17.

[43] Fang W, Ramadass P, Zhang Z. Study of internal short in a Li-ion cell II: numerical investigation using a 3D electrochemical-thermal model. J Power Sources 2014;248:1090–8.

[44] Doyle M, Fuller TF, Newman J. Modeling of galvanostatic charge and discharge of the Lithium/polymer/insertion cell. J Electrochem Soc 1993;140(6):1526–33.

[45] Fuller TF, Doyle M, Newman J. Simulation and optimization of the dual Lithium ion insertion cell. J Electrochem Soc 1994;141(1):1–10.

[46] Doyle M, Newman J. Comparison of modeling predictions with experimental data from plastic lithium ion cells. J Electrochem Soc 1996;143(6):1890–903.

[47] Chaturvedi NA, Klein R, Christensen J, Ahmed J, Kojic A. Algorithm for advanced battery management systems: modeling, estimation and control challenges for lithium ion batteries. IEEE Control Syst Mag 2010;30(3):49–68.

[48] Chaturvedi NA, Klein R, Christensen J, Ahmed J, Kojic A. Modeling, estimation, and control challenges for lithium-ion batteries. In: American control conference, Marriott Waterfront, Baltimore, MD, USA; June 30–July 02, 2010. p. 1998–2002.

[49] Klein R, Chaturvedi NA, Christensen J, Ahmed J, Findeisen R, Kojic A. Electrochemical mode based observer design for a Lithium-ion battery. IEEE Trans Control Syst Technol 2013;21(2):289–301.

[50] Han X, Ouyang M, Lu L, Li J. Simplification of physics-base electrochemical model for lithium ion battery on electric vehicle. Part II: pseudo-two-dimensional model simplification and state of charge estimation. J Power Sources 2015;278:814–25.

[51] Smith K, Wang CY. Power and thermal characterization of a lithium-ion battery pack for hybrid-electric vehicles. J Power Sources 2006;160:662–73.

[52] Fang W, Kwon OJ, Wang CY. Electrochemical-thermal modeling of automotive Li-ion batteries and experimental validation using a three-electrode cell. Int J Energy Res 2010;34:107–15.

[53] Srinivasan V, Wang CY. Analysis of electrochemical and thermal behavior of Li-ion cells. J Electrochem Soc 2003;150(1):A98–A106.

[54] Christensen J, Cook D, Albertus P. An efficient parallelizable 3D thermos-electrochemical model of a Li-ion cell. J Electrochem Soc 2013;160(11):A2258–67.

[55] Cai L, White RE. Mathematical modeling of a lithium ion battery with thermal effects in COMSOL Inc. Multiphysics (MP) software. J Power Sources 2011;196:5985–9.

[56] Song L, Evans JW. Electrochemical-thermal model of lithium polymer batteries. J Electrochem Soc 2000;147(6):2086–95.

[57] Ye Y, Shi Y, Cai N, Lee J, He X. Electro-thermal modeling and experimental validation for lithium ion battery. J Power Sources 2012;199:227–38.

[58] Electrically propelled road vehicles–battery systems–dimensions for Lithium-Ion-Cells. DIN SPEC 91252; January 2011.

[59] Material property for 1:1 EC:DEC/LiPF6 in material database of Comsol Multiphysics ver4.4; 2014.

[60] Feng X, He X, Lu L, Ouyang M. Research on simplification of simulating the heat conduction in the lithium-ion battery core. In: Presented in EVS27, Barcelona, Spain; 2013. p. 1–12.

[61] Zhang J, Wu B, Li Z, Huang J. Simultaneous estimation of thermal parameters for large-format laminated lithium-ion batteries. J Power Sources 2014;259:106–16.

[62] Feng X, Sun J, Ouyang M, He X, Lu L, Han X, et al. Characterization of large format lithium ion battery exposed to extremely high temperature. J Power Sources 2014;272:457–67.

[63] Material property for aluminum in material database of Comsol Multiphysics ver4.4; 2014.

[64] Lienhard IV JH, Lienhard V JH. Heat conduction concept, thermal resistance, and the overall heat transfer coefficient. In: A heat transfer text book, 3rd ed. Cambridge (MA): Phlogiston Press; 2008. p. 62–78 [chapter 2, sec. 1].

[65] Thermal modeling of a cylindrical Li-ion battery in 2D. User manual of comsol multiphysics, ver 4.4; 2014.

[66] Ioannou PA, Sun J. On-line parameter estimation. In: Robust adaptive control, Dover ed. Mineola (NY): Dover Publiaions, Inc.; 2012. p. 144–249 [chapter 4].

[67] Xiong R, Sun F, Gong X, et al. A data-driven based adaptive state of charge estimator of lithium-ion polymer battery used in electric vehicles. Appl Energy 2014;113:1421–33.

[68] Sun F, Xiong R, He H. A systematic state-of-charge estimation framework for multi-cell battery pack in electric vehicles using bias correction technique. Appl Energy; 2014. http://dx.doi.org/10.1016/j.apenergy.2014.12.021.

[69] Electric vehicle battery test procedures manual. USABC manual. ver2; January 1996. <http://avt.inl.gov/battery/pdf/usabc_manual_rev2.pdf>.

[70] Feng X, Fang M, He X, Ouyang M, Lu L, Wang H, et al. Thermal runaway features of large format prismatic lithium ion battery using extended volume accelerating rate calorimetry. J Power Sources 2014;255:294–301.